ELSEVIER

Nuclear Engineering and Design 186 (1998) 379–394

Nuclear Engineering and Design

Failure of Zircaloy cladding under transverse plane-strain deformation

T.M. Link [a,1], D.A. Koss [a], A.T. Motta [b,*]

[a] *The Pennsylvania State University, Department of Materials Science, University Park, PA 16802, USA*
[b] *The Pennsylvania State University Department of Nuclear Engineering, 231 Sackett Building, University Park, PA 16802–1408, USA*

Received 1 June 1998; received in revised form 18 August 1998; accepted 3 September 1998

Abstract

Experiments have been performed to examine the ductility of Zircaloy 4 cladding tubes under conditions of near plane-strain deformation in the hoop direction (transverse to the tube axis) at temperatures of 25 and 300°C and at strain rates of 10^{-3} and 10^{2} s^{-1}. To conduct these experiments, a specimen configuration was designed in which near plane-strain deformation is achieved, and a test methodology was established to determine two failure conditions: the limit strain at the onset of localized necking and the fracture strain. Experiments performed on cold-worked stress relieved material using the transverse plane-strain specimen geometry indicate major differences in failure behavior from that observed in uniaxial tension, although both test conditions result in failure by a localized necking process. The experimental results also indicate that while plane-strain fracture strains increase with temperature between 25 and 300°C, at a given temperature they are insensitive to strain rate. The limit strains at localized necking also increase with temperature but only at the high 10^{2} s^{-1} strain rate. Finally, the failure data indicate a strong sensitivity to surface flaws, as predicted by localized necking theory.

Keywords: Zircaloy; Deformation; Fracture strain; Failure data

1. Introduction

One of the postulated design-basis accidents in the licensing of light water reactors (LWR) is a reactivity initiated accident (RIA), in which a control-rod drop or control rod ejection causes a large amount of energy to be deposited in the fuel. This energy deposition causes the fuel to expand and fission gas contained in the fuel to be released (Meyer et al., 1996). Both of these factors load the Zircaloy cladding into the plastic regime and may result in its failure. Recent experiments have indicated that the energy deposition limits for cladding failure and for fuel dispersal (established for fresh cladding) may be reduced at high fuel burnup, because of a degradation in the ability of the cladding to withstand a RIA.

* Corresponding author. Tel.: +1-814-8650036; fax: +1-814-8658499.

[1] Current address: U.S. Steel Technical Center, Monroeville, PA 15146, USA.

0029-5493/98/$ - see front matter
PII: S0029-5493(98)00284-2

In order to predict cladding survivability, there has been considerable interest and effort in developing models capable of predicting cladding failure under in-service loading, similar to RIA. The accuracy of such model predictions obviously depends on appropriate and accurate failure data. Currently, there is a large body of ductility data based on uniaxial tests, performed on specimens oriented along the tube axis and also on 'ring' tests based on Zircaloy specimens oriented transverse to the tube axis. However, the direct use of such data in a mechanics-based failure analysis to predict the probability of cladding failure appears to be inappropriate given the fact that in-service loading usually subjects the cladding to hoop expansion under multiaxial tension, often under conditions where little or no extension occurs along the cladding axis. Thus, in-service cladding deformation and failure is likely to occur under conditions close to a 'transverse plane-strain' deformation path. Given the strong sensitivity of the failure of Zircaloy sheet to stress state (Yunchang and Koss, 1985), it is important to study the behavior of thin wall Zircaloy cladding under deformation conditions such as transverse plane strain.

This investigation has several goals. First, we wish to design a specimen capable of subjecting Zircaloy cladding to a deformation path similar to that experienced during a potential in-service cladding failure, such as the RIA. To this end, using both experiment and finite element analysis, we have developed a small-scale transverse plane-strain tension test configuration, which relies on a notched ring test specimen. That geometry, which is an evolution of earlier geometries (Wagoner, 1980; Kampe and Koss, 1986), and which may be thought of as a version of the localized ductility arc (LDA) specimen (Wisner and Adamson, 1996), offers the advantage that, in addition to a fracture strain, the failure strain based on the onset of localized necking can be determined. We then examined the mechanical response of cold worked stress relieved Zircaloy 4 cladding tubes using gridded transverse plane-strain specimens to determine failure characteristics as a function of (i) deformation path (uniaxial and plane-strain failure), (ii) temperature (25 and 300°C) and (iii) strain rate (10^{-3} s^{-1} and 10^{2} s^{-1}). Finally, we examine the sensitivity of plane-strain deformation to the presence of surface flaws on the basis of both experimental behavior and theoretical predictions that rely on the constitutive response of the cladding.

2. Experimental method

2.1. Material

For this study, several identical Zircaloy 4 cladding tubes were obtained from Sandvik Metals in the cold-worked, stress-relieved condition (CWSR). The tubes had an outer diameter of ≈ 9.5 mm and a wall thickness of about 0.56 mm. Measurements of the cladding wall thickness (made at fixed intervals around the circumference of the tube using a traveling microscope), show that the cladding wall thickness can vary by up to 20 μm (or 3% of the wall thickness) around the perimeter of a given section of cladding.

The grain structure was observed using light microscopy. Specimens were prepared for metallographic examination by first chemically polishing ground specimens by immersing the sample in a magnetically stirred 45% HNO_3–45% H_2O–10% HF solution for 30 s, and then anodizing in Picklesimer's solution for 30 s at 20 V dc (Danielson, 1980). This technique revealed elongated grains with approximately 10:1 aspect ratio parallel to the tube axis. The elongated grains were ≈ 10–15 μm long and 1–2 μm thick.

The Zircaloy 4 cladding studied here exhibits a crystallographic texture typical of the cold worked and stress relieved (CWSR) condition (Mahmood and Murty, 1991; Lemaignan and Motta, 1994). Fig. 1, which was generated from flattened and polished sections of the cladding, shows that the basal planes tend to align with their poles inclined $\approx \pm 40°$ to the normal of the tube surface and oriented towards the tangential direction. The prism poles show a strong tendency to align along the tube axis, which is also consistent with previous observations for such cladding. These results show that the texture in this cladding results in basal and prism pole intensities nearly ten times their random value.

2.2. Transverse stress–strain response

For in-service cladding failure of Zircaloy in which the cladding fails due to an axial split, the major strain direction is the hoop direction of the cladding tube, which is transverse to the cladding axis. Thus, transverse tension and compression tests were performed on the cladding material to determine its stress–strain–strain rate response at both 25 and 300°C.

As is common in tensile tests of Zircaloy cladding, we found that the uniform strain values were quite small (≈ 0.02) for this cold worked and stress relieved material. Thus we chose to use compression testing as the primary means to determine the transverse constitutive response of the cladding. For compression testing, small transverse samples were cut from the wall thickness of the cladding using a diamond blade wafering saw.

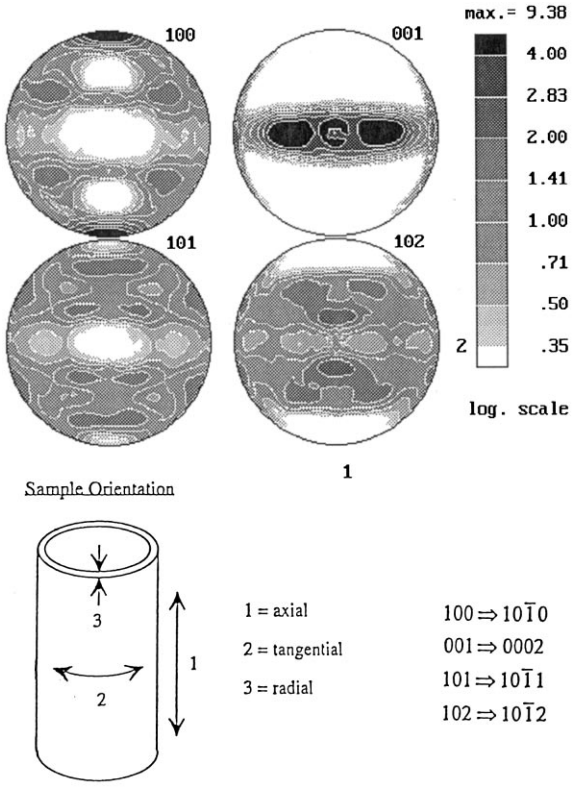

Fig. 1. Pole figures for flattened piece of the Zircaloy 4 cladding used in this study.

Each surface of the specimen was ground flat using 600 grit SiC grinding paper, and then each sample was pickled briefly in HNO_3/HF solution to remove any cold-worked surface layer. The samples were ≈ 1 mm long with widths and thicknesses ranging from 0.5–0.7 mm, care was taken to maintain a uniform cross-section area. Compression testing was performed at an initial strain rate of 10^{-3} s^{-1}. The specimen end faces in contact with the polished alumina load plates were lubricated with molybdenum disulfide to minimize friction. 'Jump tests' were also performed in order to calculate the strain rate-hardening exponent of the cladding. In these tests, the cross-head speed was instantaneously changed by a factor of ten and the corresponding change in load was recorded on both increasing and (subsequently) decreasing cross-head speeds.

In order to determine the constitutive stress–strain response of the cladding in tension, we also performed a limited number of tensile tests of cladding, which had been mechanically flattened and then machined into specimens, again with the tensile axis transverse to the cladding axis. These specimens have gauge lengths of 9 mm and gauge widths of 3 mm. Both length and width strains were monitored during deformation using the micro-hardness indentation gridding procedure described below. The tensile tests were also performed at an initial strain rate of 10^{-3} s^{-1}.

2.3. Ring tests: uniaxial tension

For uniaxial tension testing, ring stretch specimens were cut from the cladding with a reduced gauge section, as shown in Fig. 2. The gauge length was 2.1 mm long and 0.5 mm wide, and the tensile tests were also performed at an initial strain rate of 10^{-3} s^{-1}. Both length and width strains were monitored during deformation using a micro-hardness indentation gridding procedure described later.

The transverse tension testing (both uniaxial and plane-strain) of the Zircaloy cladding specimens required a gripping arrangement which maintained the circular cross-section shape of the cladding. Within the specimen gauge section, sets of die inserts and a pin-loaded grip assembly were

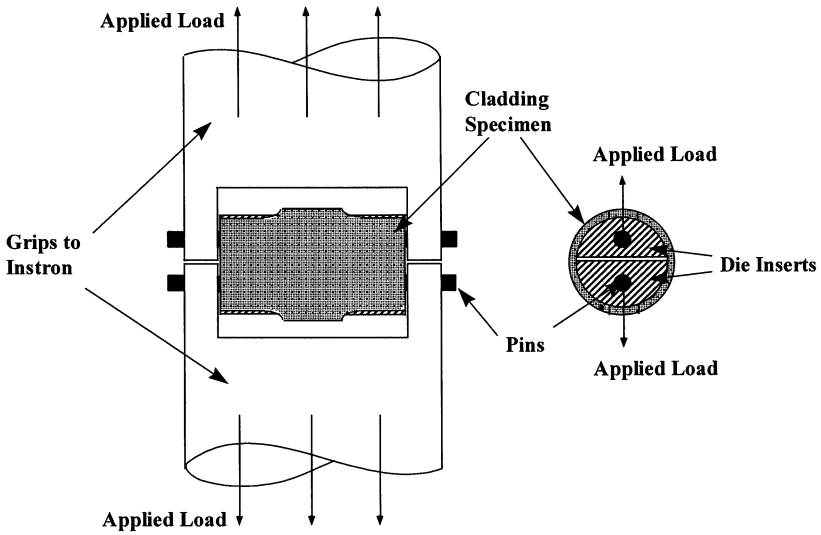

Fig. 2. Schematic representation of loading assembly designed for transverse tension testing of cladding tube specimens. Note the gauge section is on top of the die insert, to maintain constant curvature during testing; lubrication is applied between die inserts and specimen to minimize friction.

machined from 17–4 precipitation-hardenable stainless steel as shown in Fig. 2. In order to minimize the friction between the outer surface of the die inserts and the inner surface cladding specimen, the interface was lubricated with two layers of vacuum grease and two layers of Teflon tape at the beginning of each test.

The uniaxial specimen dimensions are shown in Fig. 3. It is important to note that the gauge sections of the cladding test specimens were oriented at the top and bottom of the die inserts, such that a constant specimen curvature was maintained during deformation. As is commonly done in the determination of forming-limit diagrams for sheet metal formability (Hecker, 1975), this technique relies on lubrication to minimize the friction coefficient such that load is efficiently transferred to the specimen gauge section. Furthermore it has also been shown that the limit strains at the onset of localized necking (used later in this paper as a failure condition) are independent of interface friction (Hecker, 1975). Thus our measurements of limit strain would not be affected if lubrication were not perfect.

Ring tests performed in the above manner differ from those in which the specimen gauge length is more conventionally positioned at the openings between the 'double D' die inserts. We initially performed 'conventional' tests with unlubricated

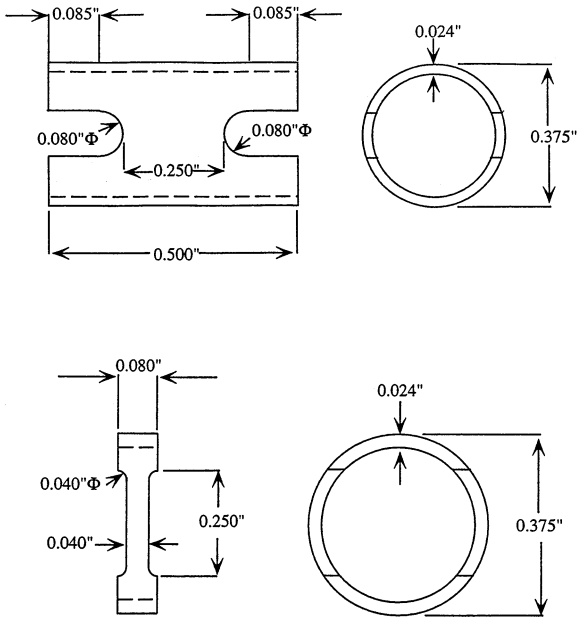

Fig. 3. The geometry of plane strain tension and uniaxial ring specimens used in this study.

specimens positioned between the die openings and found that the combination of specimen bending and friction effects yielded fracture strain data similar in magnitude to our data but with much larger scatter. Furthermore, when compared to the lubricated test configuration described above, our results indicate $< 5\%$ difference in failure loads between the two configurations, or minimal friction effects. We thus conclude that the most accurate and reproducible failure strain data was obtained with the configuration shown in Fig. 2 in which the gauge section was placed adjacent to the die inserts with lubrication being used to transfer load to the deforming section. Finally we call attention to the fact that, as is the case in obtaining forming limit diagram data, the parameters of principal interest here are strain data, not stresses, our procedure serves this goal very well.

2.4. Ring tests: transverse plane-strain tensile specimen configuration

Utilizing the die insert and lubrication procedure shown in Fig. 2, we designed the double edge notched 'transverse plane-strain' specimen configuration shown in Fig. 3. The specimen, which is a modification of a configuration developed earlier (Wagoner, 1980; Kampe and Koss, 1986) uses the constraints of the two notches to force the central region of the gauge section to deform such that there is little contraction across the specimen width during the test. Thus, a near plane-strain deformation condition is achieved. Importantly, the specimen configuration allows us to determine both the limit strain at the onset of localized necking and the fracture strain at specimen separation.

There have been previous attempts to develop specimen geometries designed for Zircaloy cladding tubes and capable of providing realistic failure strain data design and modeling purposes (Tomalin, 1977; Coffin, 1979; Adamson et al., 1986; Chung et al., 1987; Garde, 1989). For example, Adamson et al., have examined a range of subsized specimen geometries in order to characterize Zircaloy failure conditions (Adamson et al., 1986; Wisner and Adamson, 1996). In particular, these authors preferred the use of the 'localized ductility arc' (LDA) specimen which relies on a double edge notch ring geometry combined with a third notch along the surface of the specimen to impose through-thickness slip and a plane-strain deformation path. While the presence of the surface notch creates a local plane-strain condition, it immediately localizes deformation at the root of the notch. Thus, the most common failure condition used to predict failure of thin sheet metal, the limit strain at the onset of localized necking, cannot be determined.

Significant effort was employed in this study to develop a specimen geometry that subjected the cladding tube to a near plane-strain tension deformation path. Six potential specimen geometries of the shape shown in Fig. 3 were evaluated by both experiment and finite element modeling before the final specimen dimensions were determined. Potential specimens with notch diameters of 2.03, 2.54, and 3.18 mm (for a fixed ligament width of 6.35 mm) and ligament widths of 5.08, 6.35, and 7.62 mm (for a fixed notch diameter of 2.03 mm) were examined experimentally for the extent of plane-strain behavior. In these tests, both minor and major strain distributions were measured within the deforming gauge section at several interruptions during the tests and after failure. Based on the evaluation results to be described later, the specimen geometry shown in Fig. 3 (two 6.35 mm wide gauge sections flanked by 2.03 mm diameter notches) had the best performance, i.e. the minimum ratio of minor to major strain in the deforming gauge section.

Finite element modeling (FEM) was also used to evaluate the same six potential plane-strain specimens. FEM was performed using Abaqus version 5.4 to run the calculations and FEMAP version 4.1 for mesh generation and post-processing of the results. The experimentally-determined transverse stress–strain response of the cladding (see Section 3) was used in the models, and isotropic plasticity was assumed. For simplicity, flat 2-dimensional versions of the notch geometries were analyzed, and the friction between specimen and die insert (which we know is small)

was ignored. In each model, the top edge of the mesh was loaded by a fixed displacement ranging from 0.2–0.5 mm, and the resulting plastic strain distributions within the gauge section were predicted.

2.5. Measurement of strain distribution

In order to determine failure strains in terms of limit strains as well as to assess overall specimen deformation behavior, we needed to develop a technique to accurately determine strains on a local basis (as small as a 0.20 mm element) from the deforming specimens. Conventional photogridding techniques are difficult to apply to a cylindrical specimen specially one with such a small gauge section as our cladding tube specimen, and our previous experience with such grid techniques indicate that the accuracy of such grids is typically limited to ± 0.02 strain value (which introduces a large error in small strain data). As an alternative to photogridding, a process of microhardness indentation gridding was used to determine strains on a local basis. In this process, an array of two rows (spaced ≈ 1 mm apart) of 14 microhardness indents each (spaced ≈ 0.2 mm apart) was applied along the entire gauge length of each specimen before testing. A Vickers hardness indenter was used with an indenting load of 1 kg. In this case, the resulting hemispherical plastic zone is estimated to be < 30 μm or about 5% of the cladding thickness. Subsequent experimental observations showed that the indentations played no significant role in specimen deformation and that the failure path usually ignored the indentations. The distances between the indents were carefully measured for every specimen using a traveling microscope before and after testing, such that the true local strain was measured over local elements of 0.20 mm in size with an accuracy of ± 0.01 in strain value. Furthermore, interrupted testing allowed us to determine strain distributions across the entire gauge length, both prior to and including failure. Tests performed directly to specimen failure indicated no effect of the interruptions on either the limit strain or the fracture strain.

2.6. Test matrix

We tested Zircaloy-4 tube material in the plane-strain specimen configuration at two temperatures (25 and 300°C), two strain rates (10^{-3} s^{-1} and 10^{2} s^{-1}), and in some cases with different machined flaws ranging in depth from 20–80 μm. For each test we measured the strain distribution in the gauge length using the microhardness indentation method described above. The experiments in each testing condition were repeated at least three times and we report here the average results. After the initial design stage, the experimental results were found to be quite reproducible, i.e. there was not much scatter between the repeated experiments, as will be evident from the data presented below. Also in each test there was an internal verification of accuracy of our data by the fact that there were two rows of indents, each giving us two measures of the strain distribution in the gauge section per sample. As seen in the following, these sets of data are in good agreement.

3. Experimental results and discussion

3.1. Constitutive flow behavior: stress applied transverse to cladding axis

The transverse stress–strain behavior of the CWSR Zircaloy-4 cladding was determined at room temperature and 300°C by both tension and compression testing. As in previous research describing stress–strain response of Zircaloy cladding (SCDAP/RELAP5/MOD2, 1990), the stress–strain data were fitted by a 'power law' constitutive equation given by:

$$\sigma = K \varepsilon_{\mathrm{p}}^{n} \tag{1}$$

where σ is the true stress, K is the strength coefficient, ε_{p} is the true plastic strain, and n is the work hardening exponent. Fig. 4 shows experimental data and power law fits for the transverse flow behavior of the cladding at room temperature and 300°C. This figure shows that there is a significant decrease in the yield stress and flow stress of the cladding at 300°C as compared to

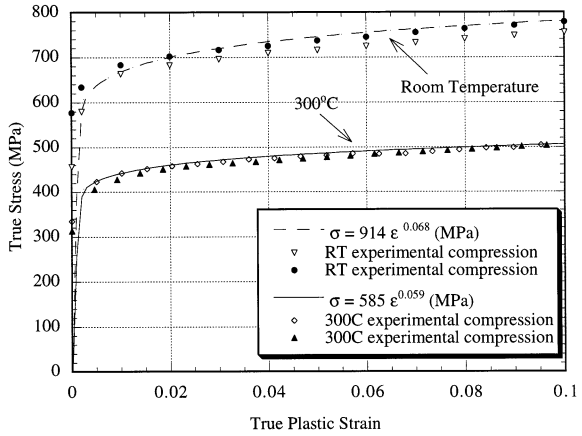

Fig. 4. Transverse stress–strain behavior of CWSR Zircaloy 4 cladding at room temperature and 300°C, as determined by two sets of compression tests (tension tests showed similar results). Also shown are the power law relationships which describe both sets of data.

room temperature. There is also a slight decrease in the overall strain hardening behavior of the cladding at 300°C as shown by the decrease in the slope of the stress–strain curve for 300°C as compared to that for room temperature. Using the true stress-true strain data from at least three tests we calculated the n and K values for CWSR Zircaloy-4 cladding, as given in Fig. 4. The values of n in the transverse direction were 0.068 at room temperature and 0.059 at 300°C. Comparing these results to previous values of $n = 0.10$ at room temperature and $n = 0.09$ at 300°C obtained for longitudinal uniaxial tests of tube specimens (SCDAP/RELAP5/MOD2, 1990), it appears the value of n in the transverse direction is smaller than the value of n in the longitudinal direction by roughly a third.

The strain-rate hardening exponent, $m = d\ln\sigma/d\ln\dot{\varepsilon}$ was also obtained by performing 'jump tests' where the cross-head speed is instantaneously changed several times during a test and the corresponding change in load is recorded. For CWSR Zircaloy-4 cladding, m was determined to be 0.018 for both room temperature and 300°C. These values correspond closely to values of $m =$ 0.02 at both room temperature and 300°C for axial tension tests of similar cladding (SCDAP/RELAP5/MOD2, 1990).

The plastic anisotropy of the cladding was measured during a uniaxial tension test in which both the specimen length and width strains were monitored using the hardness indentation grids. From these measurements, the plastic anisotropy parameter, R, was obtained in the hoop direction of the cladding as:

$$R = \frac{\varepsilon_w}{\varepsilon_t} = \frac{\varepsilon_2}{-(\varepsilon_1 + \varepsilon_2)} \quad (2)$$

where ε_w and ε_t are the width and thickness strains, respectively, and ε_1 and ε_2 are the major and minor strains in the plane of the specimen, respectively. A value of $R > 1$ indicates that through-thickness slip is more difficult than slip across the width of the specimen, which is common for Zircaloy cladding when subjected to axial tension. In our case for CWSR Zircaloy-4 cladding in the transverse direction, we determined $R = 2.3$ for room temperature, quasi-static deformation using small strain data and avoiding specimen necking. This R-value (2.3) is slightly higher than that reported (1.3) for CWSR cladding when tested in its axial direction (Delobelle et al., 1996), however, values of R as high as 6.3 have been reported for textured Zircaloy-2 sheet (Lee and Adamson, 1977). These values indicate that, at least in the unirradiated condition, through-thickness slip is relatively difficult in Zircaloy cladding. There are indications that this plastic anisotropy decreases with irradiation (Nakatsuka and Nagai, 1987; Nakatsuka, 1991).

3.2. Verification of plane-strain conditions in the gauge section

Based on isotropic plasticity, the FEM predictions consistently over predicted the degree of plane-strain constraint that was experimentally observed. For example, as shown in Fig. 5, FEM indicates that the 'best' specimen geometry (see Fig. 3) that we chose should induce plane-strain deformation (true minor strain = 0) over the central 4 mm of the gauge section. Thus, near plane-strain tension should occur over the central 60% of the specimen. In fact near plane-strain deformation was achieved only over the central 2 mm of the gauge width, which is half of that predicted

by FEM. We believe the disagreement between observation and prediction is due mainly to the plastic anisotropy of the cladding (the $R = 2.3$) and the corresponding difficulty of through-thickness slip, and the fact that the FEM code used assumed isotropic plasticity.

While agreement between FEM and experiment is limited, the experimental strain distributions show that within 2 mm wide region at the center of the specimen gauge section, the minor strain is $< 15\%$ of the major strain, which we use a our criterion for 'plane-strain' deformation. While a wider specimen would have produced a more extended region of 'plane-strain' deformation, the mechanical limitations of our grip assembly prevented testing much wider specimens. Furthermore, our grids were positioned (i.e. row of indentations 1 mm apart spanning the center of the specimen) to allow us to track deformation and fracture within the region subjected to near plane-strain deformation and to determine local values of failure/fracture strains under this deformation path. Finally, it is important to recognize that for the plane strain specimen geometry (Fig. 3) chosen, failure always initiated within the central region. Thus, our data report failure conditions for material subjected to near plane-strain deformation.

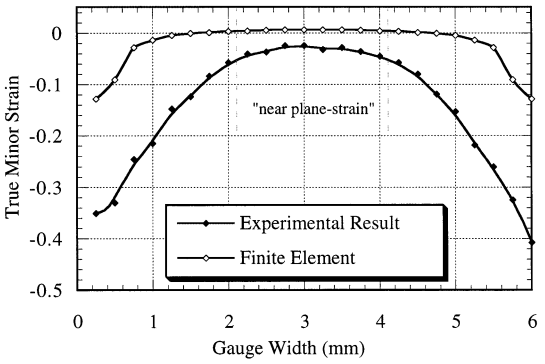

Fig. 5. Experimental measurements and finite element predictions of the width strain as a function of gauge width distance for notched plane-strain specimen. The error in the strain measurements was ± 0.01. The minor (width) strain is minimized near the center of the specimen, in agreement with FEM predictions, so that region is considered to be 'near plane strain'.

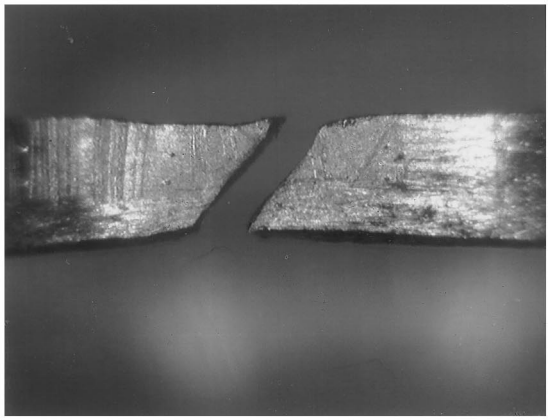

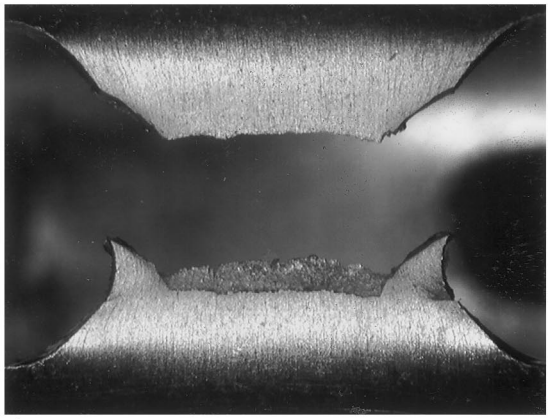

Fig. 6. Macroscopic photographs of failures of (a) uniaxial tension ring cladding specimen, where failure occurs across the width, and (b) plane-strain tension cladding specimen, where failure occurs through the thickness.

3.3. Comparison of transverse plane-strain and uniaxial tension failure

Quasi-static, transverse tension tests were performed on both uniaxial ring and notched plane-strain specimens at room temperature and 300°C. Fig. 6 shows macroscopic photographs of failed uniaxial ring and plane-strain tension specimens. As this figure shows, failure occurs due to different modes of slip in these two specimens. The notched plane-strain specimen fails due to through-thickness slip occurring on a plane inclined $\approx 45°$ through the cladding thickness,

which is consistent with the premise that cladding failure by hoop expansion must occur predominantly due to through-thickness slip. Hence, the transverse plane-strain test specimen geometry should yield data which is meaningful for failure predictions under service-like loading conditions.

In contrast to the plane-strain failure, the uniaxial ring specimens fail on a plane inclined across the width of the sample at both room temperature and 300°C, as shown in Fig. 6a. This type of failure has been observed previously in tube ductility tests at elevated temperatures (400°C), where such failures occur in spiral fashion (Garde et al., 1996). In the present case, visual examination indicates that the failure in Fig. 6a appears to have occurred as a result of a deformation localization process inclined to the stress axis. Measurements of the inclination of the failure plane across the specimen width show that failure typically occurs in the uniaxial ring specimens on a plane inclined at $\approx 41°$ to a line across the width of the specimen.

We believe that the failure path observed in Fig. 6 is consistent with thin sheet deformation and failure, and that it suggests failure due to 'localized necking'. The thin wall nature of the cladding dictates a plane-stress condition such that failure is expected to occur by localized necking. This failure mode is a consequence of 'deformation localization' and occurs within a narrow band of material such that the interface between the deforming and non-deforming material satisfies a 'line of no extension' criterion (Hill, 1952). For uniaxial tension, such a line (and therefore the localized neck) must be inclined across the specimen width. The mechanics of localized necking, which have been analyzed initially by Hill (Hill, 1952) and subsequently by others (Hutchinson and Neale, 1978; Marciniak and Duncan, 1992), specifies that the localized neck forms at a particular angle, φ^*, which is inclined across the width of the specimen. For a metal with a plastic anisotropy parameter, R, the φ^* value is given by the following relationship (Chan et al., 1984):

$$\varphi^* = 90° - \tan^{-1}\sqrt{\frac{\alpha - \left(\frac{1+R}{R}\right)}{\left(\frac{1+R}{R}\right)\alpha - 1}} \quad (3)$$

where $\alpha = \sigma_2/\sigma_1$ in which case σ_1 and σ_2 are the major and minor principal stresses. For the case of uniaxial tension, $\sigma_2 = 0$, and our degree of plastic anisotropy, $R = 2.3$, Eq. (2) indicates $\varphi^* = 40°$, which compares well with the $41 \pm 1°$ value observed experimentally. On the basis of physical observations and the characteristics of the failure, we conclude that failure of the uniaxial ring specimen is due to deformation localization in a manner that is consistent with the mechanics of localized necking. In particular, the Hill zero-extension condition, which dictates the inclination of the failure path, appears to be obeyed.

An important technological implication of the above results is that localized necking can cause failure of ring specimens of Zircaloy cladding tubes. Thus the ductility of ring specimens is limited by the onset of localized necking and the subsequent extension which is concentrated within that small zone of metal. As a result, the local strain along a ring specimen can vary greatly along its length at failure, as shown in Fig. 7. One consequence is that a value for specimen ductility becomes a function of gauge

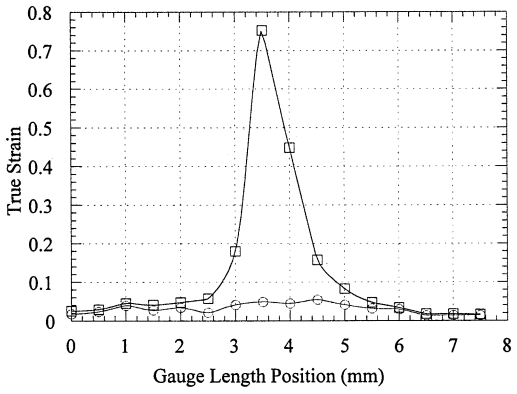

Fig. 7. Major strain distribution as a function of gauge length distance for 25°C uniaxial loading of a flattened Zircaloy specimen at two stages of the deformation process: maximum load and fracture. The error in the strain measurements was less than ± 0.01

length, increasing with decreasing gauge length especially at short gauge lengths. This effect, along with the issue of strain paths, raises serious concerns regarding the use of uniaxial ring-test ductility results in models which attempt to predict cladding failure under in-service conditions. The present results indicate that it is necessary to show in each individual case that uniaxial testing is relevant to the loading situation considered, rather than assuming this is the case.

3.4. Transverse plane-strain deformation and failure

Quasi-static (10^{-3} s^{-1}) transverse plane-strain tension tests were performed on the as-received cladding tubes at both room temperature and 300°C. Measures of the true major strain along the entire specimen gauge length (between specimen fillets) were obtained on a local basis by the microhardness gridding process. Fig. 8 shows examples of the major strain distributions for cladding tested at both room temperature and 300°C. Strain measurements were made first at interruptions during the test and then after fracture for both cases. The two sets of data for each case correspond to the two rows of microhardness indents used for strain measurements. As shown in Fig. 8, the 'limit strain' data correspond to strains measured at an interruption during the test, and the 'fracture strain' data correspond to strains measured after fracture. These two sets of strain measurements illustrate how strains initially accumulate in a uniform manner along the specimen gauge length. Then in the later stages of deformation, a decidedly non-uniform strain distribution evolves as localized necking develops within a section ≈ 1 mm long.

Treating the 0.6 mm thick cladding as a material which obeys sheet metal deformation and fracture, we define two measures of cladding ductility from the strain measurements shown in Fig. 8. First, the limit strain, defined as the plastic strain at the onset of localized necking, can be obtained either from the strains measured at the interruption in the test or from the shoulders of the strain profile at fracture. The limit strain is commonly used as the most important measure of failure strain in sheet metal deformation since relatively little extension of

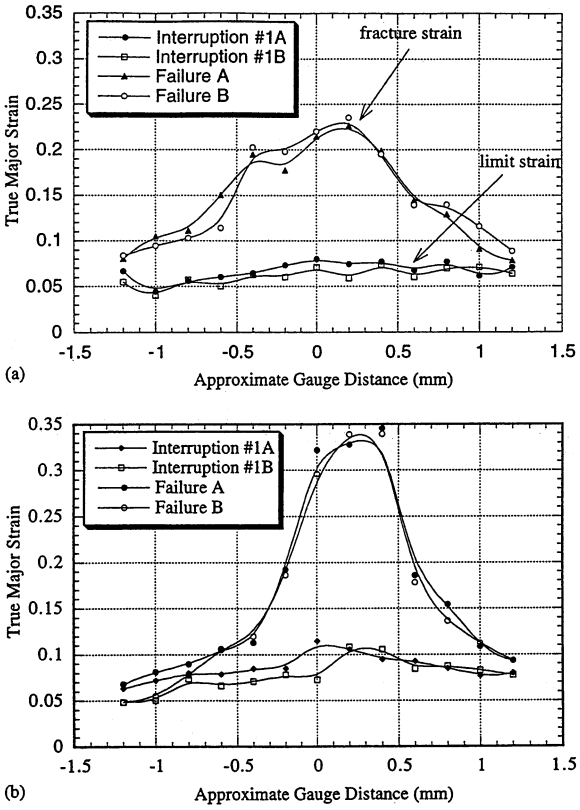

Fig. 8. Major strain distributions at maximum load and at fracture as a function of gauge length distance for (a) 25°C and (b) 300°C under quasi-static plane-strain loading. The sets of data A and B correspond to the two rows of indents. The error in the strain measurements was ± 0.01.

a large workpiece will occur before fracture beyond deformation localization, even though large local strains may subsequently accumulate within the necked region. This behavior can be seen in both Figs. 7 and 8, which illustrate the manner in which strain localizes and accumulates after the first test interruption. In general, limit strains increase with work hardening and strain-rate hardening, and they usually exhibit a minimum value under plane-strain deformation (Yunchang and Koss, 1985). Thus, we expect plane-strain deformation to be a particularly severe mode of deformation for cladding which fails due to localized necking.

The fracture strain, defined as the local strain within the necked region of the material at frac-

ture, is the second measure of cladding ductility obtained from the strain measurements. The fracture strain is determined from the strain measured at the peak of the strain profile at fracture. In general, ductile fracture strains are usually representative of the overall damage accumulation in a material and are therefore directly dependent upon factors that influence the nucleation, growth, and coalescence of voids. For example, the fracture strains should be sensitive to the presence of brittle particles, such as hydrides in Zircaloy, which lower the critical strain for both void nucleation and linking (Yunchang and Koss, 1985).

Because the limit strain is a measure of the extent to which a material deforms uniformly before localized necking occurs, limit strains account for deformation occurring throughout the entire cladding under uniform loading conditions. The fracture strains correspond to how much local strain accumulates within the necking region, thus fracture strains depend on deformation occurring in only a very localized region in the cladding. For a cladding tube experiencing load transfer around its perimeter, most of the cladding expansion will occur under the uniform strain condition (represented by the limit strain). Only a relatively small increment of cladding extension will occur after localized necking develops and strains accumulate to the fracture strain level within the specimen neck (represented by the fracture strain). From a technological standpoint of predicting overall cladding extension at failure under 'force' loading, the limit strain is a more accurate measure of ductility than a failure strain, because the latter includes the large, localized strain accumulation shown in Fig. 7. In other words, the fracture strain is a measure of the local strain at failure, and the limit strain is a measure of the overall strain that would be measured in the cladding after the test.

Fig. 9 shows the limit strain and the fracture strain for room temperature and 300°C testing under plane strain conditions at low and high strain rate, based on at least three transverse plane-strain tests per condition. As shown in Fig. 9 increasing the strain rate has minor effects on both the limit strain and the fracture strain at room temperature as well as 300°C (note: in all cases the strain reported is the maximum principal strain value). A careful examination of Fig. 8 suggests that there may be a small decrease in limit strain at the high strain rate for cladding tested at room temperature, but the other data lie within experimental error. While the strain distributions is similar to that shown in Fig. 8 for the two strain rates, at room temperature the entire strain distribution for 10^2 s^{-1} loading appears to be shifted to slightly lower strains as compared to the strain distribution at the 10^{-3} s^{-1} strain rate. With this in mind, plane-strain cladding ductility appears to be relatively insensitive to temperature in the range of 25–300°C, in view of the limit strain data.

In contrast to the relative lack of effect of strain rate on our measures of ductility, Fig. 9 also shows that increasing temperature results in a significant increase in the fracture strains at both

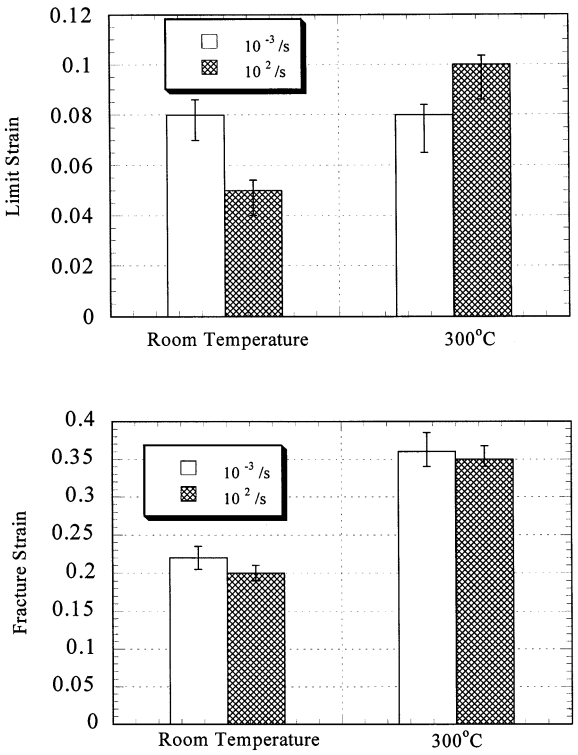

Fig. 9. Limit strains and fracture strains for Zircaloy 4 tested at low and high strain rate, and at 25 and 300°C.

low and high strain rates. On the other hand, increasing temperature has a mixed effect on limit strain behavior, causing no effect at the low strain rate of 10^{-3} s^{-1}, but resulting in an increase in the limit strain for failure at 300°C at the high strain rate(10^{2} s^{-1}). The failure/fracture load data are consistent with the trends shown in Fig. 8 with the largest effect being observed between the low strain-rate tests performed at room temperature and 300°C.

Fractography of the failed specimens shows a dimpled fracture surface characteristic of ductile fracture due to void nucleation, growth, and linking, as is typically observed for unirradiated, as-received Zircaloy cladding. In view of the damage accumulation characteristic of microvoid ductile fracture, we suggest that the increase in fracture strain observed at 300°C is likely a result of the decreased flow stress of the material at 300°C. At lower levels of flow stress, we expect the critical strain for void nucleation to increase, delaying fracture to larger strains (Yunchang and Koss, 1985).

3.5. Sensitivity of failure to surface flaws

Pettersson and co-workers recognized not only the importance of strain path on the ductility of Zircaloy failure but also observed a strong sensitivity of cladding ductility to surface flaws (Pettersson, 1974; Pettersson et al., 1979). We performed a set of systematic experiments examining the sensitivity of Zircaloy cladding to surface flaws for the transverse plane-strain deformation path. Room temperature quasi-static tests were performed on notched plane-strain specimens across the outer surface of the gauge section to measure the ductility of specimens containing shallow grooves ranging from 10–80 μm deep, parallel to the axis of the tube. We observed that failure of these grooved specimens initiated in the center of the specimen and occurred on a plane $\approx 45°$ through the cladding thickness, similar to smooth (ungrooved) specimens. As shown in Fig. 10, the presence of the surface flaw in the form of a 77 μm deep groove is very effective in localizing deformation within the groove and limiting deformation outside it. This figure also shows that the localized neck is contained almost entirely within the groove, while the regions outside of the groove experience nearly uniform deformation. Hence, fracture strains are measured using the groove itself as a gauge length, and limit strains are measured from regions outside the groove.

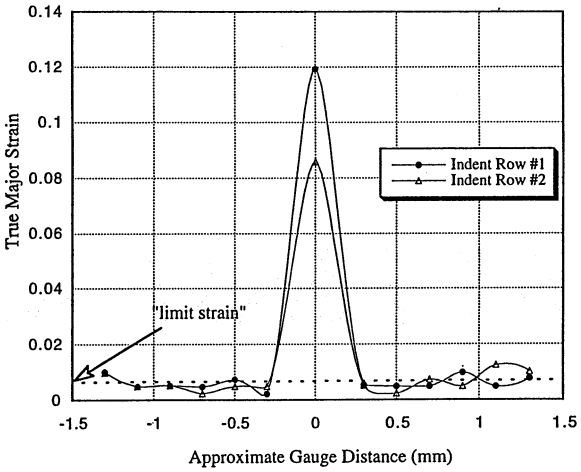

Fig. 10. The major strain distribution along the gauge length for plane-strain specimen containing a 77 μm deep machined groove ($f \cong 0.13$). The error in the strain measurements was ± 0.01.

Based on the limit strain as a measure of failure, Fig. 11 shows a strong sensitivity of the limit

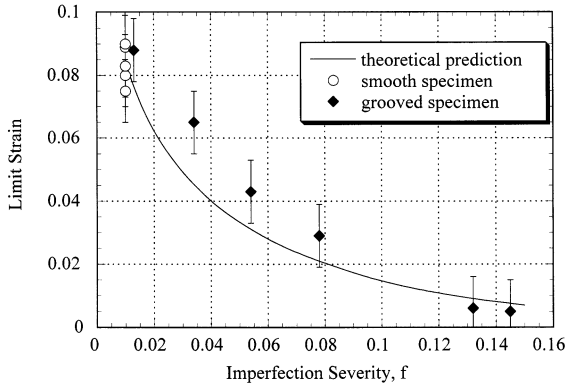

Fig. 11. Theoretical predictions and experimental results showing limit strains as a function of imperfection severity for room temperature plane-strain cladding deformation. The circles denote ungrooved specimens where the f factor was assessed from the normal variation in fabrication thickness.

strain of Zircaloy cladding tubes to the presence of small thickness flaws. Characterizing the flaw as an 'imperfection' with a severity, f, given as the ratio of groove depth to cladding thickness, we see that a 30 μm deep groove (which results in a 5% reduction of cladding thickness, $f = 0.05$) will cause a 50% reduction of the failure strains from 0.08–0.04. The data in Fig. 11 thus indicate that surface flaws which assume a linear dimension can be very effective in localizing deformation within the flawed region. From the standpoint of in-service cladding performance, such imperfections may arise from features such as non-uniform oxidation or a rim of hydrided material that fails at small strains thus creating a surface flaw capable of significantly reducing cladding extension to failure.

Previous analyses have predicted a sensitivity of sheet metal ductility to the presence of surface flaws in the form of thickness 'imperfections', such as grooves (Marciniak and Kuczynski, 1967; Hutchinson and Neale, 1978; Marciniak and Duncan, 1992; Link et al., 1997). Those analyses assume load transfer along the specimen and predict the strain evolution both within and outside of the imperfection as a function of specimen extension. The degree of the failure strain sensitivity on imperfection severity was shown to depend on the material's strain hardening and strain-rate hardening behavior as well as on the severity of the imperfection. The limit strain at the onset of localized necking within the imperfection can then be predicted from the analysis as deformation concentrates within the groove (Marciniak and Kuczynski, 1967; Hutchinson and Neale, 1978; Marciniak and Duncan, 1992; Link et al., 1997). Using such an analysis (Link et al., 1996, 1997), we have previously predicted that, given its small strain hardening exponent ($n = 0.06$–0.07), the ductility of Zircaloy cladding should be quite sensitive to surface flaws.

In this study, we used the data from our experiments to test the predictions of the imperfection theory for a plane-strain deformation path. In the analysis referred to above, the only variables are constitutive behavior of the cladding, reported earlier in this paper, and the imperfection severity (i.e. the depth of the groove. Fig. 11 compares our experimental results directly to the theoretical predictions for the onset of localized necking in specimens containing a groove-like imperfection extending across the specimen width. As shown in Fig. 11, there is good agreement between the experimental results and the theoretical analysis, as the observed loss of ductility with imperfection severity is predicted quite well by the analysis. It should also be noted that the results from several smooth test specimens have been included in this figure and are adequately predicted using an imperfection severity of 0.01. As reported earlier, thickness variations of 3% have been measured around the circumference of as-received cladding. Thus a 1% thickness imperfection may readily be assumed to exist within the notched gauge section of the cladding simply due to the cladding fabrication process. In summary, these results are consistent with plane-strain failure of cladding occurring as a result of a localized necking process. Furthermore, failure occurs in such a manner that failure strains can be predicted from existing theory which relies on the presence of a thickness imperfection as well as the strain and strain-rate hardening behavior of the cladding. Our theoretical analysis also included the effects of elastic deformation: the only effect of deformation in the elastic region was a very minor increase in the failure strain of less than 0.5% (Link et al., 1997).

The observations of Pettersson et al. (Pettersson et al., 1979) who studied the influence of irradiation on the ductility and defect sensitivity of recrystallized Zircaloy tubing can readily be understood in terms of imperfection theory. These researchers found that the ductility of the tubing subjected to plane-strain burst tests was much more sensitive to surface flaws in the irradiated condition than in the unirradiated state. Furthermore, the defect sensitivity was much reduced in tests conducted on ring specimens where the loading was uniaxial (Pettersson, 1974). The authors concluded that both the plane-strain deformation path and the low level of work hardening in the irradiated condition were important in determining defect sensitivity (Pettersson et al., 1979), which raises concerns regarding cladding performance during a RIA. In terms of the Pettersson

results, the imperfection analysis predicts a strong sensitivity of cladding ductility to small surface flaws, especially for materials of small work hardening exponent associated with reactor exposure, and subjected to a plane-strain deformation path. Thus, those results are quite consistent with our expectations.

The type of flaw described above can readily appear in irradiated cladding especially after high burnup. One possibility is uneven cladding oxidation. After a burnup of 45 GWd/ton, oxide thicknesses of 70–100 μm can exist in some types of cladding (Seibold and Woods, 1994). In that case, a 20% fluctuation in the oxide thickness could trigger the above mentioned instability if the fluctuation forms a linear defect along the tube axis. Another possibility is that a hydride rim or blister forms, possibly aided by oxide spalling. The fracture resistance of this rim would be highly dependent on the local hydride distribution, but a hydrided rim of about 50 μm seen in the HBO-1 experiment (Fuketa et al., 1996) may well be sufficient to cause cladding failure by localized necking. In contrast, the 25 μm hydride rim in HBO-3 may be an insufficient imperfection to cause failure prior to the 1.5% hoop extension during an RIA.

Finally, we make the point that our conclusions for cladding sensitivity to flaws are valid under conditions of force loading and not displacement loading. The crucial difference between the two is that in force loading there is equilibrium of forces between the thin and thick sections of the tube, while in displacement loading, there is no mechanism for load sharing, and equilibrium is not established. In the former case, load transfer favors strain localization within the cladding, while during displacement loading the cladding is constrained by the fuel to a condition of equal strain between the cladding and fuel. In this latter case, our mechanism would not be applicable, and during this type of loading the cladding would not be sensitive to the presence of flaws. At high burnup, there is considerable pellet-cladding bonding and consequently friction. As the friction increases, one goes from force loading to displacement loading. However fission gas loading would represent force loading, and the rim region may act as a lubricant between cladding and fuel during deformation. Furthermore, the types of cracking observed in the RIA testing done so far suggests a failure under conditions near those of force loading.

4. Conclusions

The deformation and fracture behavior of unirradiated Zircaloy-4 cladding has been studied under loading conditions relevant to an in-service cladding failure. Based on the theory of localized necking, computational analysis, and experimental observations, the principal results of this study are as follows:

1. A straightforward, double edge notched tensile test specimen configuration has been designed for the evaluation of cladding ductility under transverse plane-strain conditions. Both finite element analysis and experiments have been used to optimize the specimen configuration, which subjects the cladding to loading in the hoop direction under near plane-strain tension. A gridding technique has been developed to determine the local strains at specimen failure.
2. Two measures of cladding ductility have been determined: (a) the limit strain which indicates the onset of a localized necking failure; and (b) the fracture strain which indicates the local strain across the fracture surface. For the case of uniform force loading around the perimeter of a cladding tube, the limit strain is the most accurate indication of cladding extension at failure.
3. Comparisons of transverse cladding failures between plane-strain tension specimens and uniaxial tension ring specimens indicate a significant difference in failure path. The uniaxial tension specimen fails due to slip localizing across the width of the specimen, while the plane-strain specimen is forced to fail along the cladding axis due to through-thickness slip, similar to the anticipated failure of cladding during a postulated RIA. The orientations of the failure paths are consistent with failure due to a localized necking process, as has been observed in the failure of sheet metal.

4. The constitutive deformation response in the hoop orientation of cold worked and stress relieved cladding has been determined from compression tests performed under quasi-static strain rates at 25 and 300°C. In both cases, a strain-rate hardening exponent of 0.018 was obtained, the strain hardening exponent decreased slightly from 0.068 at 25°C to 0.059 at 300°C. The plastic anisotropy factor, R, was 2.3 for room temperature tensile deformation in the hoop direction of the cladding.
5. Tests performed on cladding containing linear surface flaws in the form of grooves of controlled depths indicate that the cladding ductility, as measured by the limit strain, decreases rapidly with increasing flaw depth. The experimental results can be predicted by an imperfection analysis which predicts localized necking in sheet metal of known constitutive response, deformed under a plane-strain stress state, and containing a linear imperfection in the form of a groove, a thinner section or a band of weak material.
6. The deformation localization process that causes cladding failure has been examined using interrupted testing, and measurements of local strain distributions have been performed both prior to, and after material fracture. These data indicate that the limit strain, corresponding to the onset of localized necking, is insensitive to temperature (25 vs. 300°C) at a low strain rate (10^{-3} s^{-1}) but increases somewhat with temperature at high strain rate (10^{2} s^{-1}). In contrast, the fracture strain, measured locally across the fracture surface, is insensitive to strain rate but increases with temperature.

Acknowledgements

We are indebted to Ross Bradley of Sandvik Metals for supplying the Zircaloy-4 samples for this study, and to Douglas Bates for help in conducting the experiments. We also thank Charles Roe of the Naval Surface Warfare Center at Carderock for conducting the high strain rate experiments. Thanks are also due to John Bingert of Los Alamos National Laboratory for measuring the textures reported here. Finally, we thank Ralph Meyer for his encouragement and support of this research. This research was funded by the Nuclear Regulatory Commission under Educational Research Grant NRC-04-95-068.

References

Adamson, R.B., Wisner, S.B., Tucker, R.P., Rand, R.A., 1986. Failure strain for irradiated Zircaloy based on subsized specimen testing and analysis. ASTM STP 888, 171–185.

Chan, K.S., Koss, D.A., Ghosh, A.K., 1984. Localized necking at negative minor strains. Metal. Trans. A 15A, 323–329.

Chung, H.M., Yagge, F.L., Kassner, T.F., 1987. Fracture behavior and microstructural characteristics of irradiated Zircaloy cladding. In: Seventh International Symposium on Zr in the Nuclear Industry. ASTM STP 939, 775–801.

Coffin, L.F., 1979. Localized ductility method for evaluating Zircaloy-2 cladding. ASTM STP 681, 72–87.

Danielson, P., 1980. In: Zirconium and Hafnium and their Alloys, ASM Handbook, pp. 497–501.

Delobelle, P., Robinet, P., Bouffioux, P., Greyer, P., LePichon, I., 1996. A unified model to describe the anisotropic viscoplastic Zircaloy-4 cladding tubes. In: Eleventh International Symposium on Zr in the Nuclear Industry. Garmisch-Partenkirchen ASTM STP 1295, pp. 373–393.

Fuketa, T., Nagase, F., Ishijima, K., Fujishiro, T., 1996. NSSR/RIA experiments with high burnup fuels. Nucl. Safety 37 (4), 328–342.

Garde, A.M., 1989. Effects of irradiation and hydriding on the mechanical properties of Zircaloy-4 at high fluence. In: Eight International Symposium on Zr in the Nuclear Industry. ASTM STP 1023, San Diego, CA, p. 548.

Garde, A.M., Smith, G.P., Pirek, R.C., 1996. Effects of hydride precipitate localization and neutron fluence on the ductility of irradiated Zircaloy-4. In: Eleventh International Symposium on Zr in the Nuclear Industry. Garmisch-Partenkirchen, ASTM STP 1295, 407–430.

Hecker, S.S., 1975. Sheet Metal Industries, 52. pp. 671–676.

Hill, R., 1952. J. Mech. Phys. Solids 1, 19.

Hutchinson, J.W., Neale, K.W., 1978. In: Mechanics of Sheet Metal Forming. Plenum Press, New York, 111, 127 and 269.

Kampe, S.L., Koss, D.A., 1986. The effect of stress state on the hydrogen embrittlement of Ni. Acta Metal. 34, 55–61.

Lee, D., Adamson, R.B., 1977. Modeling of localized deformation in neutron irradiated Zircaloy2. ASTM STP 633, 385–401.

Lemaignan, C., Motta, A.T., 1994. Zirconium in nuclear applications. In: Frost, B.R.T. (Ed.), Nuclear Materials. VCH, New York, pp. 1–52.

Link, T.M., Koss, D.A., Motta, A.T., 1997. On the influence of an embrittled rim on the ductility of Zircaloy cladding. In: ANS International Topical Meeting on Light Water Reactor Fuel Performance. Portland, OR, ANS, pp. 634–642.

Link, T.M., Motta, A.T., Koss, D.A., 1996. On the Issue of Zircaloy Ductility During a Reactivity Initiated Accident. In: Twenty-Fourth Water Reactor Safety Information Meeting. NUREG/CP0157, Bethesda MD, p. 141.

Mahmood, S.T., Murty, K.L., 1991. Effect of tensile deformation on crystallographic texture in Zircaloy sheet. In: Ninth International Symposium on Zr in the Nuclear Industry. ASTM STP 1132, Kobe, Japan, pp. 119–139.

Marciniak, Z., Duncan, J., 1992a. In: Arnold, E. (Ed.), Mechanics of Sheet Metal Forming. London.

Marciniak, Z., Kuczynski, K., 1967, International Journal Mechanics Science 9, p. 609.

Meyer, R.O., McCardell, R.K., Chung, H.M., Diamond, D.J., Scott, H.H., 1996. A regulatory assessment of test data for reactivity initiated accidents. Nucl. Safety 37 (4), 271–288.

Nakatsuka, M., 1991. Mechanical properties of neutron irradiated fuel cladding tube, J. Nucl. Sci. Technol. 28(4) 356–368.

Nakatsuka, M., Nagai, M., 1987. Reduction of plastic anisotropy of Zircaloy cladding by neutron irradiation, I: yield loci obtained from knoop hardness. J. Nucl. Sci. Technol. 24 (10), 823–838.

Pettersson, K., 1974. AE-488.

Pettersson, K., Vesterlund, G., Andersson, T., 1979. Philadelphia, ASTM ASTM-STP 681, p. 155.

SCDAP/RELAP5/MOD2, 1990. Code Manual volume 4: MATPRO: A Library of Materials Properties for Light WaterReactorsAccidentAnalysis NUREG/CR-5273, EG-2555, chapter 4.9.

Seibold, A., Woods, K.N., 1994. In: Proceedings of ANS International Topical Meeting on LWR Fuel Performance. ANS West Palm Beach, pp. 633–642.

Tomalin, D.S., 1977. Localized ductility of irradiated Zircaloy-2 cladding in air and iodine environments. ASTM STP 633, 557–572.

Wagoner, R.H., 1980. Measurements and analysis of plane–strain work hardening. Metal. Trans. A 11A, 165–175.

Wisner, S.B., Adamson, R.B., 1996. Combined effects of radiation damage and hydrides on the ductility of Zircaloy-2. GE Fuel 3, 1–21. (and accepted for publication in Nuclear Engineering And Design, 1998)

Yunchang, F., Koss, D.A., 1985. Metal. Trans. A 16A, 675.